Fuel 345 (2023) 128265

Contents lists available at ScienceDirect

Fuel

journal homepage: www.elsevier.com/locate/fuel

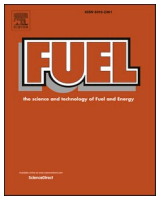

Full Length Article

Impact of prechamber design and air–fuel ratio on combustion and fuel consumption in a SI engine equipped with a passive TJI

Emmanuele Frasci [a,*], Ricardo Novella Rosa [b], Benjamín Plá Moreno [b], Ivan Arsie [a], Elio Jannelli [a]

[a] Department of Engineering, University of Naples "Parthenope", Centro Direzionale – Isola C4, 80143 Napoli, NA, Italy
[b] CMT – Motores Térmicos, Universitat Politècnica de València, Camino de Vera, 46022 Valencia, Spain

ARTICLE INFO

Keywords:
Passive turbulent jet ignition
Lean combustion
Engine modeling
Combustion modeling
Prechamber geometry
Optimal prechamber design

ABSTRACT

The increasing concern about Greenhouse Gas (GHG) emissions led the European Union to introduce increasingly stringent limits to the CO_2 from road vehicles, with an impact on the sales of passenger cars. Vehicles equipped with Spark-Ignition (SI) engines became more numerous than those equipped with Compression-Ignition (CI) engines, due to the expensive aftertreatment system needed to comply with the restrictive European emission standards. However, SI engines provide lower efficiency than CI engines, due to the low compression ratio and the operation with a stoichiometric air–fuel ratio. Lean combustion can be a solution to increase SI engines' efficiency. Nevertheless, extremely lean mixtures lead to an increase in Cycle-to-Cycle Variability (CCV).

The prechamber ignition concept, also known as Turbulent Jet Ignition (TJI), is an attractive solution for lean combustion, without its drawbacks. There are two ways to implement this concept: active TJI and passive TJI. In active TJI, there is an additional fuel supply system inside the prechamber, while passive TJI operates without additional injection. Therefore, passive TJI offers advantages in terms of simplicity, easy packaging, and low cost.

In this work, the effects of passive TJI on combustion and performance are investigated by simulation analyses. Particularly, a 1-D engine model was developed to simulate the TJI combustion and validated against the experimental data. Furthermore, model simulations were carried out to assess how the prechamber geometry, in terms of A/V ratio, affects the jet performance, main chamber combustion, and fuel consumption, for different λ values.

The analysis was conducted in a medium-to-high speed and load operating condition, namely 4500 rpm and 13 bar of Indicated Mean Effective Pressure (IMEP), under both stoichiometric and lean mixture. Simulation results demonstrated that the best jet performance and the highest engine efficiency are obtained for medium-to-high values of prechamber volume and large diameters, both in stoichiometric and lean-burn conditions, defining a common optimum prechamber design regardless of the λ level.

1. Introduction

Nowadays, the transport sector is going through an important turning point. The increasing concern about climate change, of which Greenhouse Gas (GHG) emissions are considered the main responsible, is pushing political institutions like the European Union to introduce increasingly stringent limits to the CO_2 emitted by road vehicles [1]. Therefore, car manufacturers are forced to develop new technologies to meet these regulations, while ensuring adequate engine performance at a reasonable cost. Spark-Ignition (SI) engines represent the main propulsion system for passenger cars, as they require cheaper aftertreatment systems to fulfill the European emissions standards if compared to Compression-Ignition (CI) engines. However, SI engines provide lower efficiency, and then lower fuel economy, than CI engines [2]. The main reasons are the low compression ratio (between 8 and 12) and the need to operate the engine with a stoichiometric air–fuel ratio (λ = 1.0). The latter is needed to guarantee an adequate flame speed, to ensure a stable combustion process [3], and the use of the Three-Way Catalyst (TWC) [4]. A viable solution to improve the thermal efficiency of a SI engine is lean combustion, which consists in operating the engine with lean mixtures (i. e. λ greater than 1.0) [5]. The lean-burn operation allows reducing heat losses through the combustion

* Corresponding author.
E-mail address: emmanuele.frasci001@studenti.uniparthenope.it (E. Frasci).

https://doi.org/10.1016/j.fuel.2023.128265
Received 24 January 2023; Received in revised form 27 March 2023; Accepted 29 March 2023
Available online 3 April 2023

chamber walls, increases the ratio of the specific heats (γ), and reduces pumping losses at part load [6]. However, the actual TWCs are not able to deal with lean mixtures [7] and then the imposed NO_x emissions limit can be only achieved at very high air–fuel ratios ($\lambda = 1.8 \div 2.0$) [8]. Moreover, extremely lean mixtures result in ignition and flame propagation issues [9], promoting Cycle-to-Cycle Variability (CCV) and increasing the probability of misfire, with an unavoidable impact on HC emissions [10].

In this context, the prechamber ignition concept, also known as Turbulent Jet Ignition (TJI) [11–13], represents a very promising solution for enabling the implementation of the aforementioned strategies, without their drawback in SI engines [14,15]. TJI concept uses a conventional spark plug to ignite the air/fuel mixture inside the prechamber, which is connected to the main chamber through a set of orifices [16]. The pressure increase resulting from the prechamber combustion process determines the ejection of a set of turbulent and reacting jets towards the main chamber, forcing the combustion onset in multiple locations, and sweeping the main chamber volume [17].

The characteristics of turbulent jets have been discussed in the literature [18,19]. Allyson et al. [20] studied the kinematics and the development of the reacting jets. TJI promotes very fast combustion in the main chamber and reduces the relative importance of CCV, especially under lean mixtures, if compared to a conventional spark-ignition system [21]. Faster combustion also allows for reducing the knock tendency, thus enabling the increase of the compression ratio to further improve engine thermal efficiency [22].

There are two different approaches to implement the TJI concept, namely active and passive [11,12]. In active TJI [23], the prechamber is equipped with an additional fuel supply system, that allows direct control of the air–fuel ratio inside the prechamber, independently from that in the main chamber.

In passive TJI systems [24], there is no additional fuel injection system inside the prechamber, so its air–fuel ratio cannot be directly controlled. Nevertheless, passive TJI offers advantages in terms of simplicity, easy packaging, and low cost, as the prechamber can be mounted instead of the conventional spark plug. However, the passive TJI deals with some issues, like the prechamber filling and scavenging, so the limits of the concept in terms of maximum air and/or EGR dilution should be still investigated.

The TJI concept has been widely investigated [25]. Particularly, the increased combustion velocity [26,27] and its capability to operate under lean mixtures [28] make the active TJI concept an attractive technology to improve engine thermal efficiency while reducing pollutant emissions [29].

However, the extra cost of the fuel supply system inside the prechamber and the related control compromises its employment in passenger cars, where the packaging and manufacturing costs are critical issues.

For this reason, the passive TJI concept seems to be a very promising solution to overcome these limitations, while decreasing fuel consumption and pollutant emissions in new SI engines [25,30]. The advantages of the passive TJI in terms of faster combustion have been analyzed in [31] and [32], by assessing the impact of the concept under both air and EGR dilution, while in [33] the performance of different passive prechamber configurations is analyzed in detail, together with the air/EGR dilution limits.

In this paper, the effects of the passive TJI concept on the combustion process both in stoichiometric and lean-burn operating conditions have been experimentally and numerically assessed. The results of the experimental campaign have been used to validate a 1-D engine model. Like in [33], the combustion process in the main chamber has been simulated through a quasi-dimensional predictive combustion model, able to simulate the dynamics of the turbulent reacting jets from each prechamber nozzle and the subsequent flame front propagation from the tip of each jet.

Furthermore, model simulations have been carried out to investigate the impact of the prechamber geometric characteristics, namely the prechamber volume and the nozzle diameter, on the jet performance (mainly in terms of jet penetration) both in stoichiometric and lean-burn conditions, starting from a base prechamber configuration. Although a similar analysis has been carried out in [33], in the current work the predictive main chamber combustion model allows evaluating in detail the impact of the prechamber geometry on the combustion process inside the cylinder, as well as on engine performance and fuel consumption.

The experimental campaign has been carried out on a single-cylinder SI engine. The tests have been performed at 4500 rpm and 13 bar of Indicated Mean Effective Pressure (IMEP), increasing the relative air–fuel ratio (i. e. λ) from 1.0 to 1.6, to assess the benefits of the passive TJI concept under lean mixture conditions.

2. Experimental layout

2.1. Engine and test bench characteristics

The experimental tests have been carried out on a single-cylinder research version of a four-stroke turbocharged SI engine, well representative of those employed for new passenger cars. The most important engine technical data are listed in Table 1.

The original Gasoline Direct Injection (GDI) fuel supply system has been replaced by a Port Fuel Injection (PFI) system, assembled in the intake manifold at 270 mm from the cylinder head, to obtain a homogeneous air–fuel mixture. The cylinder head is equipped with four valves, actuated by a double-overhead camshaft (DOHC). The valve overlapping has been intentionally removed, to avoid short-circuit losses.

The engine is assembled into a fully instrumented test bench, depicted in Fig. 1.

Boost conditions are simulated employing an external compressor, while the exhaust backpressure is reproduced and controlled using a throttle valve installed in the exhaust line, after the exhaust settling chamber. There is also a low-pressure EGR system, designed to provide arbitrary levels of cooled EGR even at very high intake boost pressures [33].

Water and oil cooling circuit temperatures are controlled by an AVL 577 conditioner. The fuel consumption is monitored using an AVL 733 gravimetric dynamic fuel meter, while fuel temperature is controlled by an AVL 753 conditioner. Furthermore, a calibrated gasoline with 95 Research Octane Number (RON95) is used during the tests.

Pollutant emissions are measured by a Horiba MEXA 7100 gas analyzer. Particularly, CO, CO_2, O_2, HC, NO_x, and EGR rate measurements are performed, while soot emissions, traced by the Filter Smoke Number (FSN), are measured by an AVL 415 Smoke meter. In-cylinder air–fuel ratio is measured by the Horiba MEXA 7100 gas analyzer and by a UEGO sensor in the exhaust line [33].

In-cylinder pressure is measured by a piezoelectric sensor, while intake and exhaust pressures are measured by piezoresistive sensors. All the high-frequency signals are sampled with a resolution of 0.2°CA. During the tests, 250 cycles have been acquired for all the operating conditions.

Table 1
Engine technical data.

Engine	Four-stroke SI
Number of cylinders [-]	1
Displacement [cm^3]	404
Bore – Stroke [mm]	80.0 – 80.5
Compression ratio (geometric) [-]	13.4:1
Valvetrain [-]	DOHC
Number of valves/cylinder [-]	2 intake, 2 exhaust
Fuel injection system [-]	PFI ($p_{inj,\ max}$ = 6 bar)

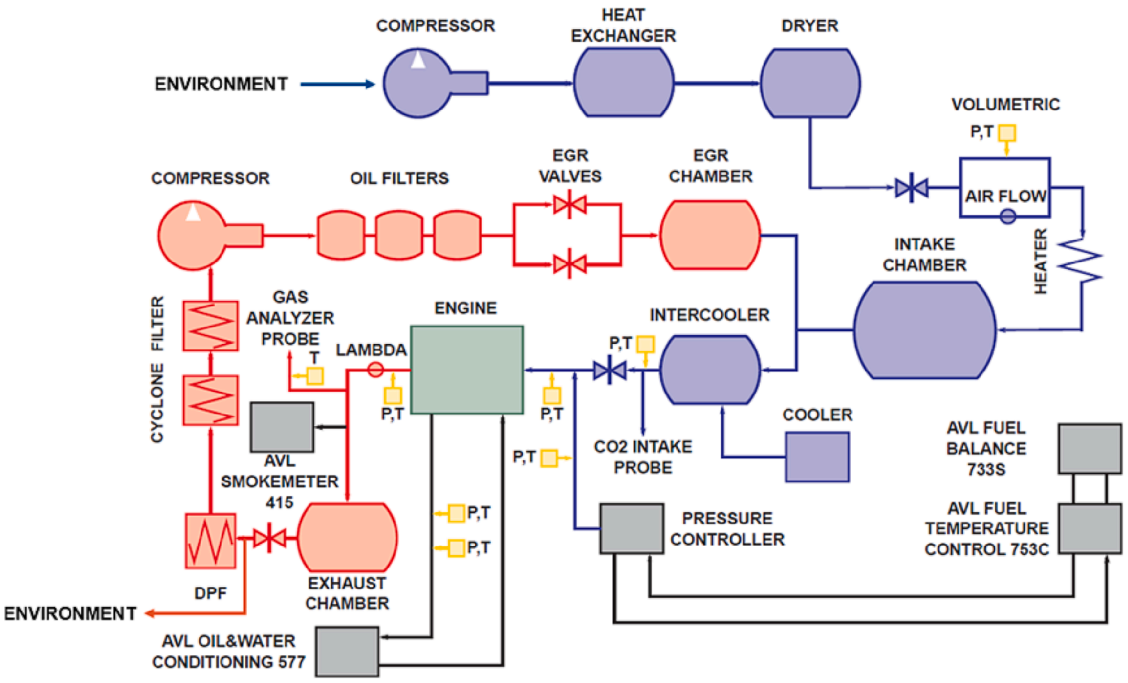

Fig. 1. Schematic of the engine test bench [33].

2.2. Prechamber description

During the experiments, a passive prechamber is used instead of the conventional spark plug. This prechamber is designed to be mounted in the same housing as the conventional spark plug in the cylinder head, being easy and quick to exchange between concepts and/or pre-chambers. The geometrical features of the prechamber used in this study, together with the ratio between the total area of the nozzles and the prechamber volume (A/V), are listed in Table 2.

2.3. Operating conditions

In the present study, an operating condition at high engine speed (4500 rpm) and high load (around 13 bar IMEP), with different λ values is considered, since one of the goals is to assess the model accuracy in predicting the effects of mixture leaning on engine performance and combustion process. Particularly, the mixture leaning is obtained through a higher air flow, achieved by increasing the intake pressure, while keeping constant the injected fuel quantity per cycle. Moreover, the spark timing was set at the Maximum Brake Torque (MBT) for all the λ values investigated.

Such a condition was chosen since high speeds compromise the scavenging and filling of the prechamber, which is critical in passive prechamber configurations. Moreover, the high load would be useful to assess the impact of the passive prechamber on the knock tendency, at different air–fuel ratios.

The details of the operating conditions investigated are listed in Table 3.

Table 2
Main geometrical features of the passive prechamber.

Volume [mm^3]	600
Hole diameter [mm]	0.7
Number of holes [-]	6
A/V [m^{-1}]	3.9

Table 3
Operating conditions investigated.

	λ = 1.0	λ = 1.2	λ = 1.4	λ = 1.6
Engine speed [rpm]	4500	4500	4500	4500
IMEP [bar]	12.7	13.2	13.3	12.6
COV_{IMEP} [%]	0.75	9.58	9.99	5.94
Injected fuel [mg/cycle]	28.5	28.5	28.5	28.5
Intake air temperature [K]	289.86	291.75	292.91	294.58
Intake pressure [bar]	1.101	1.292	1.501	1.720
Intake air mass flow rate [kg/h]	56.5	67.0	78.0	90.6
Exhaust pressure [bar]	1.062	1.206	1.386	1.531
Coolant and oil temperature [K]	350	350	350	350

3. Engine model development

A 1-D model of the test bench and the single-cylinder engine, described in section 2, was developed within the commercial software GT-Power [34], with particular attention on the combustion sub-model, described in the following section.

3.1. Combustion sub-model

The engine used for the tests, as stated above, is equipped with a passive prechamber. Therefore, there was no need to simulate the injection inside the prechamber. Like in [29] and in [35], the prechamber combustion was simulated through a Wiebe function, whose tuning was performed by matching the prechamber CA50 approximately with the main chamber Start Of Combustion (SOC) and imposing the value of prechamber combustion duration for each λ value, as no experimental data were available for the prechamber. Particularly, the prechamber combustion duration has been fixed at 4°CA for the cases with λ = 1.0 and λ = 1.2, at 5°CA for λ = 1.4, and at 6°CA for λ = 1.6, according to 3D-CFD simulation results in [32].

Regarding the main chamber combustion process, it was simulated through a multi-zone predictive model embedded within the software, able to describe the evolution and burning of the turbulent reactive jet from each prechamber nozzle and the subsequent flame propagation. Some details about the phenomenology and the modeling approach are

reported in the following.

At the beginning of the process, all the mass inside the cylinder is contained in a single thermodynamic zone, namely the main unburned zone. The fresh charge entering from the intake ports is added to this zone. The main unburned zone exchanges mass and energy with the prechamber through its holes. Once the combustion starts inside the prechamber at the spark timing, a new thermodynamic zone, the jet zone, develops in the cylinder from each prechamber orifice. The jet dynamics inside the main chamber are described by two quantities, namely the penetration distance s(t)and the tip velocity u(t) [36]:

$$S(t) = C_s t^{1/2} \left(\frac{u_{noz} d_{noz}}{C_d} \sqrt{\frac{\rho_{noz}}{\rho_{cyl}}} \right)^{1/2} \tag{1}$$

$$u(t) = C_u t^{-1/2} \left(\frac{u_{noz} d_{noz}}{C_d} \sqrt{\frac{\rho_{noz}}{\rho_{cyl}}} \right)^{1/2} \tag{2}$$

where t is the elapsed time [s], u_{noz} is the velocity at the prechamber nozzle [m/s], d_{noz} is the nozzle diameter [m], C_d is the nozzle discharge coefficient, ρ_{noz} is the fluid density inside the jet at the nozzle exit and ρ_{cyl} is the density of the charge inside the main chamber [kg/m^3]. C_s and C_u are model's tuning parameters. Particularly, the term $\sqrt{\frac{\rho_{noz}}{\rho_{cyl}}}$ in Eqs. (1) and (2) states that the greater the density at the nozzle outlet compared to in-cylinder density, the greater the jet penetration inside the main chamber.

As the jet enters the cylinder, it slows down and expands by entraining mass from the surrounding fluid. Assuming the momentum conservation, the mass entrained by the jet is given by:

$$m_{je}(t) = C_e m_{noz} \left(\frac{u_{noz}}{u(t)} - 1 \right) \tag{3}$$

where m_{noz} is the mass in the jet at the prechamber nozzle exit [kg] and C_e is the entrainment rate multiplier, a model parameter that considers transient effects in the entrainment process which cannot be explicitly modeled [34,35].

The charge entrained by the jet undergoes an ignition delay modeled by an Arrhenius-like equation [34]:

$$\tau_{ign} = C_i \rho^{-1.5} \exp\left(\frac{T_a}{T} \right) [O_2]^{-0.5} \tag{4}$$

where τ_{ign} is the ignition delay [s], ρ is the jet density [kg/m^3], T_a and T are the activation temperature (set at 3500 K) and the jet temperature [K], respectively, and $[O_2]$ is the oxygen concentration. C_i is the ignition delay multiplier. Equation (4) states that the ignition delay inside the jet decreases as the jet temperature and the oxygen concentration increase. Once the ignition takes place inside the turbulent jet, a burned zone develops in the main chamber. Initially, a fraction of the mass entrained by the jet is set aside for premixed combustion, whose rate is controlled by chemical kinetics and is calculated as follows [34]:

$$\frac{dm_{pm}}{dt} = C_{pm} m_{pm} k \left(t - t_{ign} \right)^2 f([O_2]) \tag{5}$$

where m_{pm} is the premixed mass [kg], k is the turbulent kinetic energy [m^2/s^2], t and t_{ign} are the elapsed time and the ignition time [s], respectively, and C_{pm} is the premixed combustion rate multiplier. As can be seen, the premixed combustion rate increases as the turbulence level and the oxygen amount increase.

After the ignition, the jet continues to entrain mass based on Equations (1), (2), and (3). Particularly, the combustion inside the jet is diffusive and the burn rate (dm_{jb}/dt) is calculated as follows [35, 36]:

$$\frac{dm_{jb}}{dt} = C_{df} m_{ju} \frac{\sqrt{k}}{V_{cyl}^{1/3}} f([O_2]) + \dot{s}_f m_{ju} \tag{6}$$

$$\frac{dm_{ju}}{dt} = \frac{dm_{je}}{dt} - \frac{dm_{jb}}{dt} \tag{7}$$

$$\dot{s}_f = \frac{1}{m_u} \frac{dm_{fb}}{dt} \tag{8}$$

where m_{je} is the mass entrained by the jet [kg], m_{ju} and m_{jb} are the unburned and the burned mass inside the jet, respectively, m_u is the total unburned mass in the main chamber, k is the turbulent kinetic energy [m^2/s^2], V_{cyl} is the cylinder volume [m^3] and C_{df} is the diffusive combustion multiplier. The term $\frac{\sqrt{k}}{V_{cyl}^{1/3}} f([O_2])$ is a mixing-controlled burn rate, that depends on turbulence level in the cylinder and on the stoichiometry of the mixture in the reactive jet [36]. The function $f([O_2])$, dependent on the oxygen concentration, states that an increase in oxygen amount results in a higher burn rate. Finally, $\dot{s}_f$ is a source term that couples the burning process within the jet with the combustion behind the flame front, as part of the mass entrained by the jet can be entrained and then burned by the flame front. m_{fb} is the mass burned by the flame front.

Once the reactive jet is fully developed, a spherical turbulent flame front develops at the tip of the jet. Therefore, the TJI concept involves two combustion modes that can be simultaneously active in certain instants of main chamber combustion, so a quasi-dimensional framework has been applied. Particularly, the burning by the flame front propagation is modeled by a turbulent entrainment process, followed by the combustion [37,38]. The flame front is initiated at a fixed location inside the main chamber. Moreover, the number of ignition sites within the cylinder is the same as the number of turbulent reactive jets.

The flame front propagating in the main chamber entrains mass from the surrounding environment, which is burned by the flame with a characteristic timescale. Such phenomenon is described by the following equations [34,35]:

$$\frac{dm_{fu}}{dt} = \rho_u A_e S_T - \frac{dm_{fb}}{dt} \tag{9}$$

$$\frac{dm_{fb}}{dt} = \frac{m_{fu}}{\tau} + \dot{s}_j m_{fb} \tag{10}$$

$$\tau = C_{tls} \frac{\lambda}{S_L}; \dot{s}_j = \frac{1}{m_b} \frac{dm_{jb}}{dt}; S_T = S_L + C_{tfs} u' \tag{11}$$

where Eq. (9) governs the entrainment rate of the mixture inside the main chamber by the flame front and Eq. (10) governs the burning rate of the entrained mass. m_{fu} is the unburned mass entrained by the flame front, ρ_u is the unburned mixture density, A_e is the entrainment surface area, S_L and S_T are the laminar flame speed and the turbulent flame speed, respectively (their calculation is shown in [34]), and τ is the burning characteristic timescale. The term $\dot{s}_j m_{fb}$ considers the fraction of the mass entrained by the flame front that can be entrained and then burned inside the jet. The source term $\dot{s}_j$ couples the flame propagation model with the jet combustion model.

The time constant τ and the turbulent flame speed S_T depend on the main chamber turbulence parameters, namely the turbulence intensity u' and the Taylor microscale $\lambda = L_i/Re_T$, where L_i is the turbulence integral length scale and Re_T is the turbulent Reynolds number. L_i and u', in their turn, are calculated by the turbulence sub-model in the main chamber [39].

The tuning parameters of the flame front propagation model are the dilution effect multiplier C_{de}, which takes into account the dilution of the fresh charge by residual gases and acts on S_L, the turbulent flame speed multiplier C_{tfs}, which instead affects S_T, and the Taylor length scale multiplier C_{tls}, which affects the Taylor microscale of the turbulence λ. The latter, in turn, influences the time constant of the combustion process τ (Eq. (11)) [34].

Since the main chamber combustion is assumed to start as jet-

shaped, a transition function is implemented within the model, to consider the evolution from the surface area of the jet to the spherical area of the flame front [35].

3.2. Heat transfer sub-model

The heat transfer in the main chamber has been simulated by a modeling approach based on the Woschni heat transfer correlation [40]. The heat transfer simulation approach in the prechamber is similar to that adopted for the main chamber. Particularly, the heat transfer coefficient is derived from the cylinder connected to the prechamber by calculating an area-weighted average of the head surface heat transfer coefficient. A similar approach has been adopted also for the prechamber wall temperature [29].

3.3. Model parameters' identification

According to the previous section, the main chamber predictive combustion model accounts for 7 tuning parameters, namely C_e, C_i, C_{pm}, C_{df}, C_{de}, C_{tfs} and C_{tls}, to which the duration of the Wiebe function for the prechamber combustion is added. Their identification has been carried out through a genetic algorithm-based procedure, which minimizes the

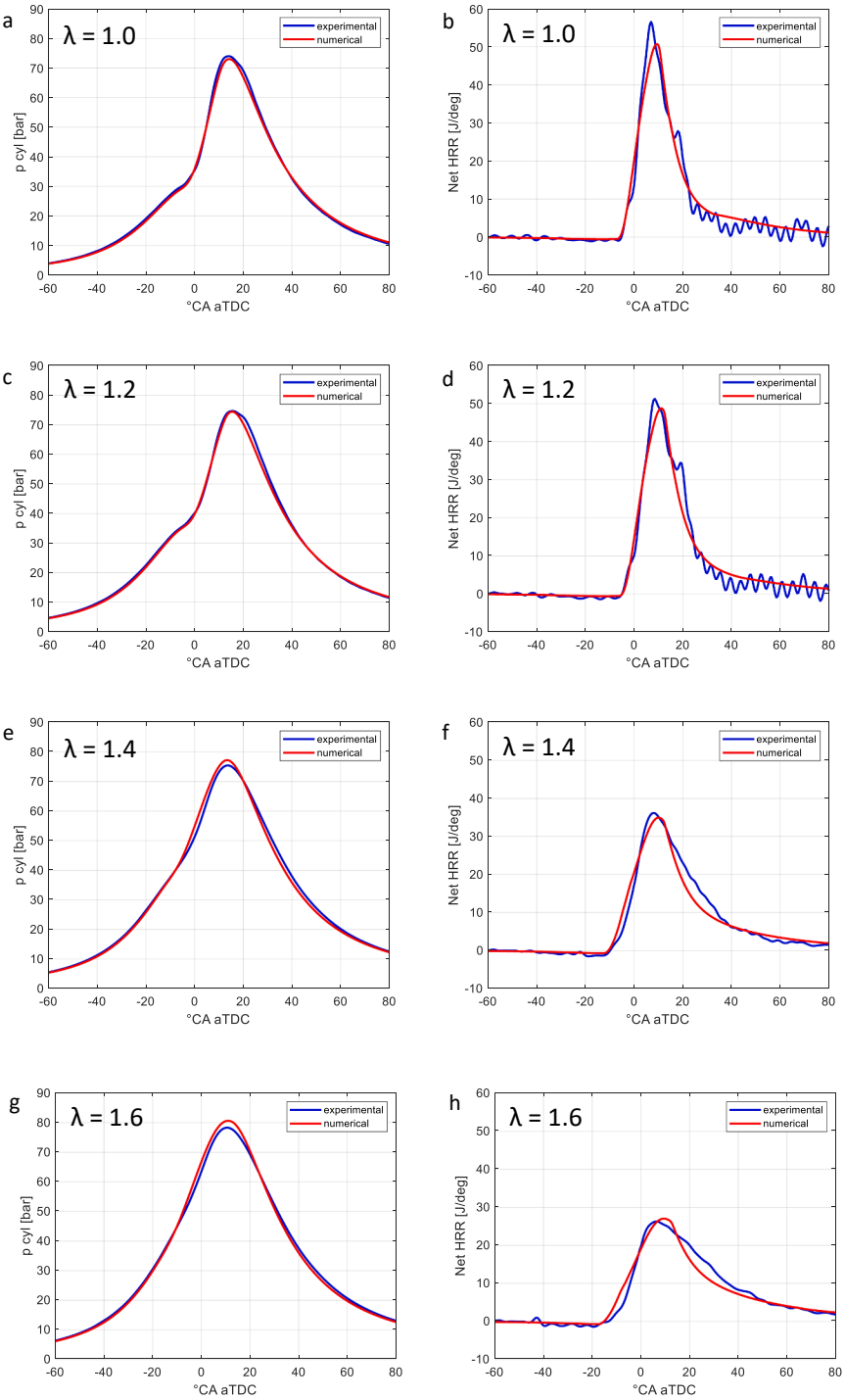

Fig. 2. Comparison between the experimental and numerical in-cylinder pressure and net HRR traces at 4500 rpm, for different λ values.

root mean square error between the measured and predicted heat release rates. Particularly, each case has been optimized independently, so a different set of all the model tuning parameters has been identified for each λ value.

In a further step, the mean of the values of C_{df}, C_{tfs} and C_{tls} identified in the four cases has been imposed for all the cases, as such parameters have shown to be almost constant with λ. In fact, those parameters affect the turbulence inside the jet (C_{df}) and in the main chamber (C_{tfs} and C_{tls}), which in turn is more influenced by the engine speed than by the air–fuel ratio.

The remaining tuning parameters, namely C_e, C_i, C_{pm}, and C_{de} have been chosen independently for each case, as they are more sensitive to the mixture composition in the turbulent jet (C_e, C_i, and C_{pm}) and in the main chamber (C_{de}), rather than to the speed. The mixture composition, in turn, is strongly influenced by the air dilution level, thus by the λ value.

4. Results and discussion

4.1. Combustion model validation

Main chamber combustion model validation has been performed by comparing simulation results and experimental data in the operating conditions reported in Table 3. Fig. 2(a ÷ h) shows the comparison of in-cylinder pressure and net HRR traces for all the investigated test cases.

From the in-cylinder pressure (Fig. 2a, c, e, and g), as λ is increased from 1.0 to 1.6, it is possible to note an increase of the maximum pressure, together with its shift towards the Top Dead Center (TDC). The former is ascribable to the increased intake pressure to obtain the mixture leaning, while the latter is due to the more advanced spark timing. However, mixture leaning results in slower combustion, which can be noted from the reduction of maximum HRR for increasing λ (Fig. 2b, d, f, and h). This is due to the reduction of laminar flame speed for leaner mixtures, which in turn is due to the higher relative importance assumed by the heat losses with respect to the energy released by chemical reactions [2]. Moreover, the reduction of the initial slope of the HRR traces for increasing λ evidences a slowdown of the jet combustion. This trend is more evident when sweeping λ from 1.2 to 1.6. This can be ascribable to the advancing of the spark timing for increasing λ, which results in a reduction of the fuel mass trapped inside the prechamber at the Start of Combustion (SOC). The latter, in turn, leads to a reduction of the energy available for the ejection, then to a reduced jet penetration [33].

However, the adoption of a passive TJI concept instead of a conventional spark ignition system allows for obtaining a faster combustion process, particularly in the case of a highly diluted mixture, thus resulting in higher in-cylinder pressure and HRR.

In Fig. 2a good agreement between experimental data and simulation results can be observed. However, the maximum in-cylinder pressure is slightly overestimated in cases with $\lambda = 1.4$ and $\lambda = 1.6$ (Fig. 2e and 2g). This may be due to the choice of the same value of the model tuning parameters acting on the turbulent flame propagation, namely C_{tfs} and C_{tls}, for all the λ values investigated. Furthermore, the predicted maximum HRR seems to be more shifted towards the expansion stroke than the experimental one for all the λ values. Particularly, the maximum value of the predicted HRR is slightly lower than that recorded during the experimental campaign in cases with $\lambda = 1.0$ and $\lambda = 1.2$ (Fig. 2b and 2d), evidencing an underestimation of the flame front propagation velocity by the model. This is also probably ascribable to the choice of the same values of C_{tfs} and C_{tls} for all the investigated cases.

Furthermore, slight differences between experimental and simulated HRR can be found in cases with $\lambda = 1.4$ and $\lambda = 1.6$ (Fig. 2f and 2h), in the first phase of the main chamber combustion process. Particularly, the initial slope of the simulated HRR is higher than the experimental one, indicating that the model slightly overestimates the jet combustion velocity.

Fig. 3(a ÷ c) shows the comparison between measured and simulated IMEP, Indicated Specific Fuel Consumption (ISFC), and CA50. In both cases, the IMEP and ISFC are calculated starting from the in-cylinder pressure signal, while the CA50 is obtained from the burned fuel fraction curve. It is worth noting that the experimental burned fuel fraction is obtained from the measured in-cylinder pressure, whereas the simulated one is predicted starting from the in-cylinder pressure, temperature, and composition (equivalence ratio, residual mass fraction, etc.) at the start of combustion.

Particularly, the IMEP (Fig. 3a) experiences an increase as λ is swept from 1.0 to 1.2, then it remains almost constant from $\lambda = 1.2$ to $\lambda = 1.4$, and finally it decreases as λ is increased up to 1.6. This trend can be explained by the way adopted to increase λ. In fact, as mentioned in Section 2.3, the mixture leaning has been obtained by keeping the fuel mass injected per cycle constant, while increasing the air mass flow rate by the intake pressure, which resulted in the increased IMEP from $\lambda = 1.0$ to $\lambda = 1.2$. On the other hand, the combustion slowdown, caused by the lean-burn operation, resulted in the performance reduction observed when sweeping λ from 1.4 to 1.6. Moreover, Fig. 3a shows a good model's accuracy in predicting the IMEP. However, the IMEP is slightly overestimated in the stoichiometric case, while it is underestimated in cases with $\lambda = 1.4$ and $\lambda = 1.6$. This behavior could be due as well to the choice of keeping constant C_{tfs} and C_{tls} for all the cases. In fact, observing Fig. 2e and g, the predicted in-cylinder pressure is slightly higher than the experimental one around the TDC in cases with $\lambda = 1.4$ and $\lambda = 1.6$, resulting in higher compression work, then in lower indicated performance.

As regards the experimental ISFC (Fig. 3b), it decreases as λ is swept from 1.0 to 1.2, remains almost constant for λ between 1.2 and 1.4, and then increases as the mixture is further leaned up to $\lambda = 1.6$, in line with the bespoken IMEP decay for the same relative air–fuel ratios. The lowest fuel consumption, then the highest efficiency, is achieved for λ between 1.2 and 1.4. In line with the IMEP prediction, the ISFC is slightly underestimated by the model at $\lambda = 1.0$, while it is overestimated at $\lambda = 1.4$ and $\lambda = 1.6$, evidencing a faster efficiency decay as the mixture is leaned out if compared to the experimental observations. Moreover, according to the simulation results, the lowest fuel consumption is achieved for $\lambda = 1.2$.

Observing Fig. 3c, it can be noted that mixture leaning results, as expected, in a more delayed combustion phasing (i. e. CA50). Particularly, the increase of the experimental CA50 is almost linear with λ. This is ascribable to the bespoken reduction of laminar flame speed for leaner mixtures, which results in slower flame propagation, in addition to the reduction of the fuel mass inside the prechamber at SOC, due to the more advanced spark timing as λ increases. However, the TJI allows obtaining a combustion phasing closer to the TDC than a conventional SI especially under lean mixtures [32], highlighting the ability of this concept to promote faster and more stable combustion also under highly diluted operating conditions. The model accurately predicts the CA50 in all the investigated cases. Slight overestimations can be observed for $\lambda = 1.0$ and $\lambda = 1.2$.

4.2. Effect of the air–fuel ratio

Once the combustion model has been validated, the reference prechamber A/V ratio (see Table 2) has been considered to assess the impact of the air dilution on the prechamber performance.

The results of this analysis are presented in Fig. 4(a ÷ c).

The maximum Δp between the prechamber and the main chamber is directly related to the capability of the turbulent reactive jets to penetrate the main chamber. Therefore, the higher Δp, the less time is needed by the jets to sweep the main chamber. The amount of fuel trapped inside the prechamber at the spark timing, referred as fuel @SOC, indicates the maximum amount of energy that can be obtained from the prechamber combustion for the jet ejection. Finally, the maximum jet

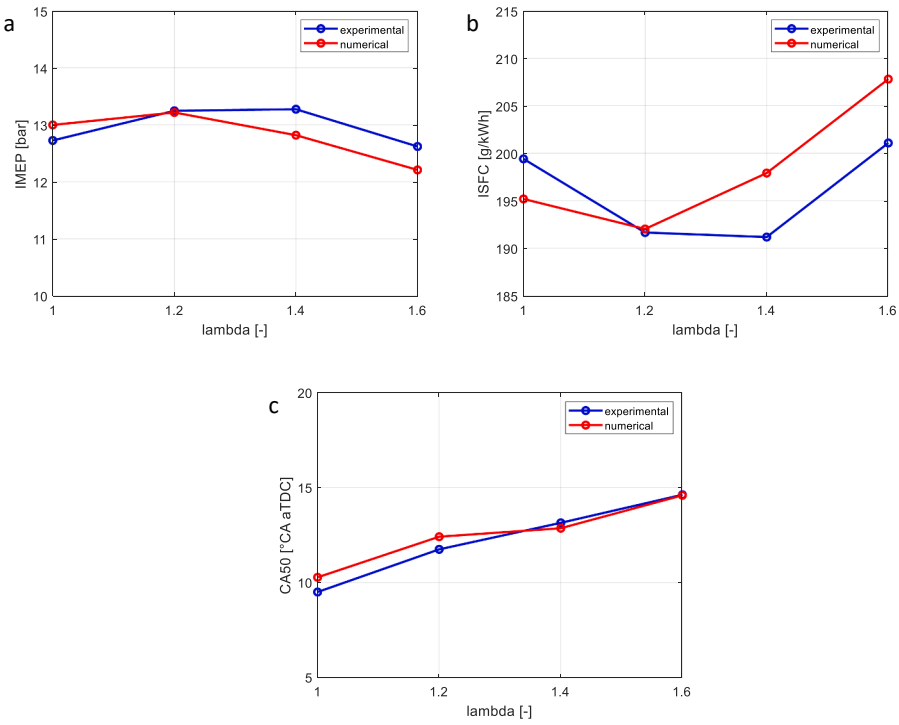

Fig. 3. Comparison between the experimental and numerical IMEP (a), ISFC (b), and CA50 (c) at 4500 rpm, for different λ values.

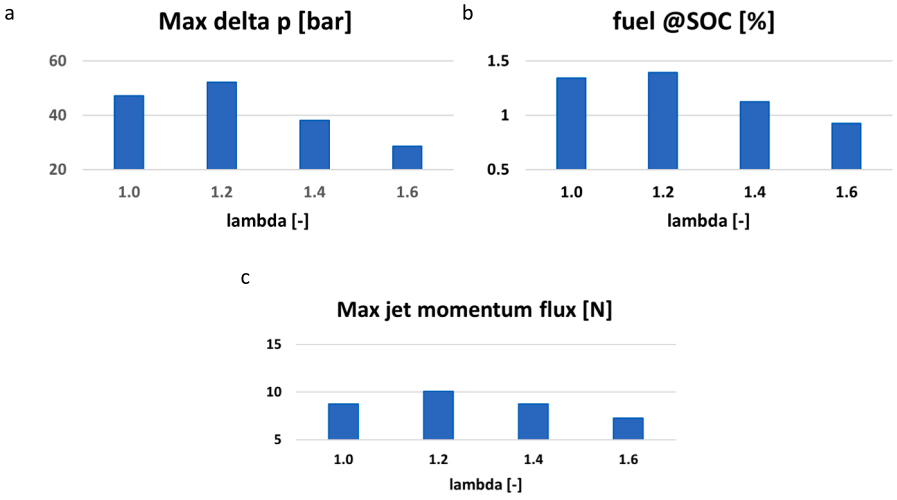

Fig. 4. Maximum Δp (a), fuel @SOC (b), and maximum jet momentum flux (c) at 4500 rpm, for different λ values.

momentum flux gives an insight of the maximum jet tip velocity, and then the jet penetration inside the cylinder.

From Fig. 4a, it is possible to note that the maximum Δp experiences a slight increase when λ is increased from 1.0 to 1.2, and then it rapidly decreases when λ is further increased up to 1.6, evidencing a decay of the jet's capability to penetrate the main chamber as the mixture is leaned out.

The behavior of the maximum Δp is directly related to the fuel @SOC (Fig. 4b), expressed as a percentage of the injected fuel mass per cycle. In fact, the fuel inside the prechamber at the spark timing affects the prechamber HRR, that in turn influences the Δp between the prechamber and main chamber. Therefore, a greater fuel amount in the prechamber at the SOC results in a faster combustion, that in turn determines a higher pressure rise rate, thus a higher maximum Δp. Particularly, the fuel @SOC slightly increases when λ is swept from 1.0 to 1.2, probably due to the higher intake pressure, which results in higher in-cylinder pressure during the compression stroke, thus forcing a greater fuel amount in the prechamber. Then, as expected, the fuel @SOC decreases when λ is increased up to 1.6, due to the advancement of the spark timing as the mixture is leaned. In fact, the SOC in the prechamber determines an increase in prechamber pressure, that prevents the prechamber from filling during the compression stroke. Therefore, a shift of the spark timing towards the compression stroke results in a lower fuel amount inside the prechamber at the SOC, then in a decrease of the energy available for the ejection of the turbulent reactive jet.

As regards the maximum jet momentum flux (Fig. 4c), its behavior is directly affected by the maximum Δp (Fig. 4a), as the jet tip velocity is controlled by the pressure difference between the prechamber and main

chamber. In fact, higher pressure difference during the ejection results in higher jet velocity and momentum, then in better jet penetration. Therefore, increasing λ from 1.0 to 1.2 results in a higher maximum jet momentum, thanks to the higher fuel @SOC. However, the maximum jet momentum decreases as λ is increased from 1.2 to 1.6, resulting in a worse jet penetration, due to the lower fuel @SOC for leaner mixtures.

Fig. 5(a, b) shows the trapped mass and the residual mass fraction inside the prechamber at the start of combustion.

The trapped mass (Fig. 5a), like the fuel @SOC (Fig. 4b) increases when sweeping λ from 1.0 to 1.2, and then it slightly decreases if λ is increased up to 1.6, justifying the behavior of the maximum Δp and the maximum jet momentum (Fig. 4a and c). On the other hand, the residual mass fraction in the prechamber at the start of combustion (Fig. 5b) experiences an opposite behavior and decreases as the mixture becomes leaner, especially when λ is increased from 1.0 to 1.2. This may be ascribable both to the leaner mixture and to the higher intake pressure as λ is increased, which promotes the prechamber scavenging.

4.3. Effect of prechamber design

Once the reference prechamber configuration has been assessed, the impact of the variation of the A/V ratio has been evaluated through further model simulations. Particularly, a variation of ± 30% in the prechamber A/V ratio, thus in both the volume and nozzle diameter, around the base value (see Table 2) has been considered, while the number of holes has been kept constant.

The maximum and minimum values of prechamber volume and nozzle diameter, together with the correspondent values of the A/V ratio, are listed in Table 4.

It is worth noting that the reduction in the geometric compression ratio induced by the prechamber is below 2.2 % for the largest prechamber volume, namely 780 mm^3, which would have negligible effects on thermodynamic efficiency.

4.3.1. Effect of prechamber volume variation

Firstly, the effect of the variation of the prechamber volume on the jet performance, while keeping constant the nozzle diameter, has been assessed for all the λ values investigated. Particularly, increasing the prechamber volume at constant nozzle diameter results in a reduction of the A/V ratio.

In Fig. 6(a ÷ c) are represented the maximum Δp, the fuel @SOC, and the maximum jet momentum flux as a function of the prechamber volume, at constant nozzle diameter (d_{nozzle} = 0.7 mm), for all the λ values investigated.

From Fig. 6a, for each λ value, it can be noted that the reduction of the A/V ratio leads to a decrease in maximum Δp. On the other hand, the fuel @SOC (Fig. 6b), as expected, increases almost linearly with the prechamber volume, at constant λ, due to the greater amount of fresh mixture that can enter the prechamber during the compression stroke. Finally, the maximum jet momentum flux (Fig. 6c) features the same behavior as the maximum Δp (Fig. 6a), in line with what is observed in Fig. 4, as the pressure difference between the prechamber and main chamber affects the jet velocity. However, at constant λ, the jet momentum seems to be not very sensitive to the variation of prechamber volume. This may be ascribable to the opposite trends featured by the maximum Δp and the fuel @SOC. In fact, while a decreasing Δp results in a reduction of the jet velocity, an increase of the fuel @SOC could lead to higher energy available for the ejection, then to an increase in the jet momentum.

Table 4
Maximum and minimum values of prechamber volume and nozzle diameter.

	Min	Base	Max
Prechamber volume [mm^3]	420	600	780
Nozzle diameter [mm]	0.49	0.7	0.91
A/V [m^{-1}]	2.7	3.9	5.0

Furthermore, increasing λ at constant volume, the behaviors of maximum Δp, fuel @SOC, and jet momentum are similar to those depicted in Fig. 4 for the reference prechamber design.

Particularly, for the smaller prechamber volume (420 mm^3), a greater sensitivity of maximum Δp to λ can be noted (Fig. 6a), especially when it increases over 1.2. This is ascribable to the higher relative importance assumed by the prechamber combustion duration at high A/V ratios.

In fact, a lengthening of prechamber combustion, occurring for higher λ values, leads to an increase in the fuel losses across the holes, especially for high values of the nozzle total area.

Fig. 7(a ÷ c) shows a comparison between the cases with λ = 1.0 and λ = 1.6 of the curves of Δp, jet mass flow rate, and jet momentum flux at constant nozzle diameter (d_{nozzle} = 0.7 mm), for different volumes.

Fig. 7a confirms the decrease of maximum Δp for lower A/V ratios. Moreover, it is worth noting that the increase in prechamber volume results in a higher negative Δp during the prechamber filling over the compression stroke. In fact, a smaller volume can be filled more rapidly than a bigger one, thus reducing the pressure difference between the prechamber and main chamber throughout the filling process. This is in accordance with the decrease of maximum Δp observed in Fig. 6a, as a higher negative Δp during the prechamber filling results in a lower Δp during the ejection. This happens because a higher negative Δp during the filling corresponds to the loss of a greater energy amount through the orifice, otherwise available for the jet ejection. This behavior is in accordance with what reported by Shah et al. [41], despite their work deals with an active TJI concept.

The Δp seems to have the same behavior for both λ values. However, as expected, the Δp traces are more shifted towards the compression stroke for λ = 1.6, due to the more advanced spark timing. Moreover, the lower fuel @SOC in the leanest case leads to a reduction of the maximum Δp with respect to the stoichiometric one. Furthermore, at equal prechamber volumes, the negative Δp during the prechamber filling is higher in the case with λ = 1.6, due to the higher in-cylinder pressure during the compression stroke (Fig. 2). The higher negative Δp during the prechamber filling, achieved for increasing prechamber volume in both cases, results in a higher (negative) mass flow rate through the orifices (Fig. 7b). On the other hand, the jet mass flow rate during the ejection, in particular its maximum value, increases as the prechamber

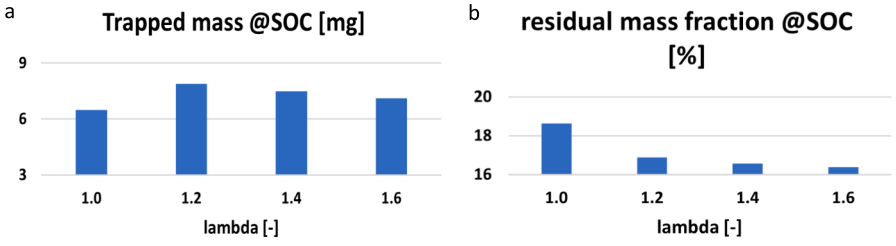

Fig. 5. Trapped mass @soc (a) and residual mass fraction @soc (b) at 4500 rpm, for different λ values.

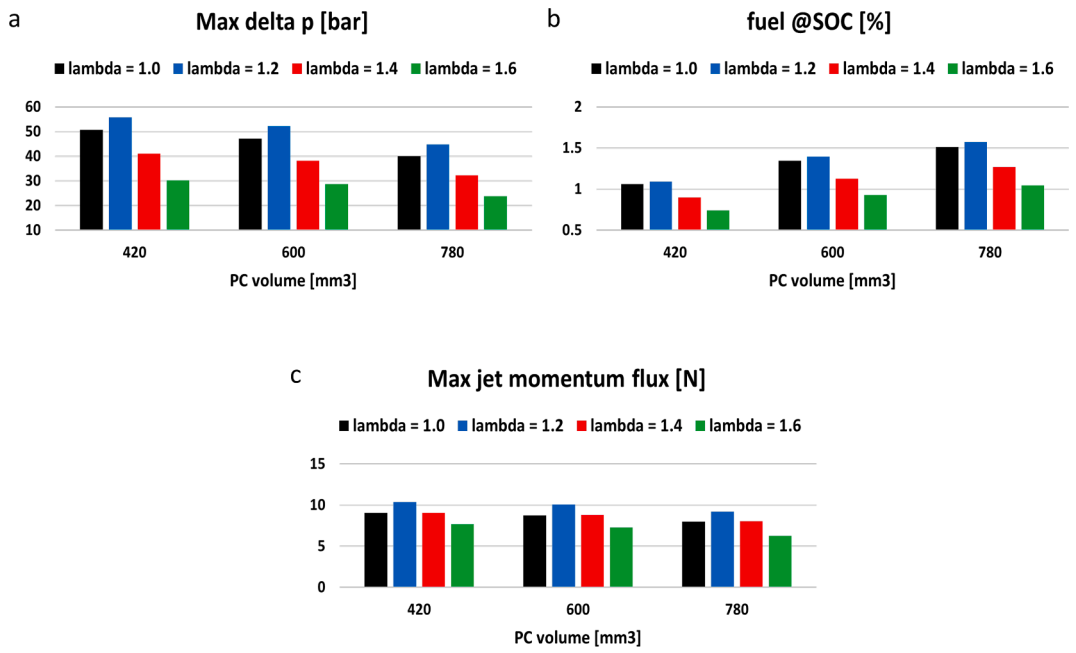

Fig. 6. Maximum Δp (a), fuel @SOC (b), and maximum jet momentum flux (c) for different values of prechamber volume, $d_{nozzle} = 0.7$ mm, at 4500 rpm and for different λ values.

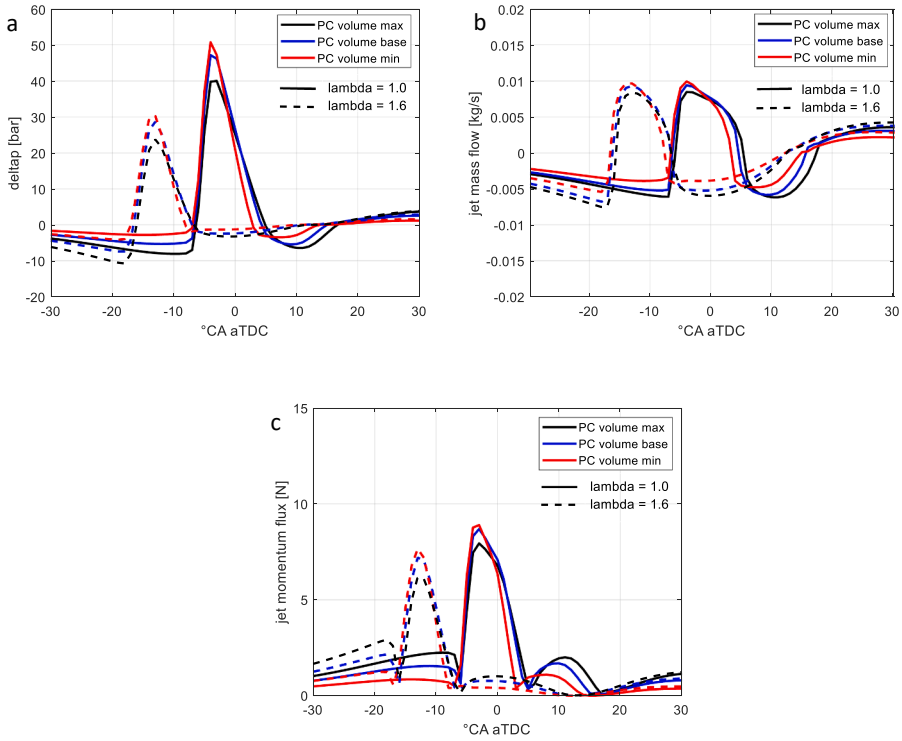

Fig. 7. Δp (a), jet mass flow rate (b), and jet momentum flux (c) for different values of prechamber volume, $d_{nozzle} = 0.7$ mm, at 4500 rpm, $\lambda = 1.0$, and $\lambda = 1.6$.

volume decreases, due to the higher maximum Δp achieved for smaller volumes (Fig. 6a). Moreover, it can be observed that the ejection process, represented by the positive values of jet mass flow rate, experiences the shortest duration for the smallest volume and the longest one for the biggest volume. This can be explained considering that the higher maximum Δp, promoted by smaller volumes, results in a better jet penetration, which in turn leads to an earlier start of combustion in the main chamber, thus to a shorter duration of the ejection process. As regards the jet momentum flux (Fig. 7c), for both λ values the second peak, related to the ejection process, slightly decreases as the volume is increased, denoting a worsening of jet penetration. Moreover, the higher negative Δp during the filling process, achieved for bigger prechamber volumes, justifies the higher jet momentum flux during this phase, evidenced by the first peak in the plots in Fig. 7c, for the base and maximum volume. This behavior is particularly evident at $\lambda = 1.6$, as the negative Δp is higher than in the stoichiometric case.

4.3.2. Effect of nozzle diameter variation

In a second step, the impact of the variation of prechamber nozzle diameter around the reference value, at constant volume, has been investigated, which leads to higher total area of the holes, thus higher A/V ratios.

Fig. 8(a ÷ c) depicts the maximum Δp, the fuel @SOC, and the maximum jet momentum flux as a function of the nozzle diameter, at constant prechamber volume ($V_{PC} = 600$ mm^3), for all the λ values.

The maximum Δp (Fig. 8a) increases for increasing A/V ratios and for each λ value, differently from what has been observed at constant diameter (Fig. 6a). Moreover, the maximum Δp seems to be very sensitive to the diameter's variation, especially when the diameter is increased from 0.49 mm to 0.7 mm.

As regards the fuel @SOC (Fig. 8b), it increases for increasing diameters, as the prechamber filling during the compression stroke is promoted by larger A/V ratios. Moreover, it is worth noting that, at constant volume, the behavior of fuel @SOC is in accordance with the maximum Δp trend, as a greater fuel amount results in a higher HRR, then in a faster pressure rise inside the prechamber. Finally, the maximum jet momentum flux (Fig. 8c) increases when the nozzle diameter is swept from the minimum to the maximum value, in line with the increase of both maximum Δp and fuel @SOC. Moreover, for each λ value, the jet momentum seems to be very sensitive to the nozzle diameter. In fact, the adoption of larger nozzle diameters at constant volume promotes the prechamber filling, maximizing the fuel @SOC, that in turn results in higher energy available for the ejection, then in better jet performance.

Also in this case, increasing λ at constant nozzle diameter, a similar trend of maximum Δp, fuel @SOC, and maximum jet momentum to the reference prechamber geometry (Fig. 4) can be observed. This happens, because the fuel @ SOC is strongly influenced by the prechamber SOC, thus by the spark timing, which is advanced as the mixture is leaned out.

Nevertheless, the fuel @SOC (Fig. 8b) shows a slightly higher sensitivity to the air dilution as the A/V ratio is increased, which in turn leads to a higher sensitivity to λ also for the maximum Δp (Fig. 8a) and the maximum jet momentum (Fig. 8c).

Fig. 9(a ÷ c) depicts the curves of Δp, jet mass flow rate, and jet momentum flux at constant volume ($V_{PC} = 600$ mm^3), for different nozzle diameters, at $\lambda = 1.0$ and $\lambda = 1.6$.

As expected, the Δp during the ejection process (Fig. 9a) increases for higher A/V ratios, especially when sweeping the diameter from the minimum to the base value, confirming what is observed in Fig. 8a. This happens for both λ values investigated. Moreover, the negative Δp during the prechamber filling increases when the nozzle diameter is reduced, especially from the base to the minimum value. The high negative Δp observed for the minimum diameter justifies the very low maximum Δp of this configuration, if compared to the others (Figs. 8a and 9a), evidencing that low A/V ratios prevent a correct prechamber filling.

This behavior is particularly evident for $\lambda = 1.6$ and is in accordance with the very low maximum Δp if compared to the other λ values (Fig. 8a). This happens, because of the higher in-cylinder pressure during the compression stroke in the leanest case, due to the higher intake pressure to obtain the air dilution, which leads to higher Mach numbers in the nozzles, thus preventing the prechamber filling.

On the other hand, the increase in prechamber nozzle diameter, thus in the prechamber A/V ratio,

results in an improvement of the ejection process, as evidenced by the huge increase in the jet mass flow rate for both λ values (Fig. 9b).

It is worth noting that the jet mass flow rate is much more sensitive to the nozzle diameter variation, rather than to the volume variation (see Fig. 7b). This happens because a variation in nozzle diameter produces a higher variation in the A/V ratio than the prechamber volume.

Furthermore, a reduction of nozzle diameter results in a longer ejection process for both λ values. However, unlike the prechamber volume, a variation in the nozzle diameter has a greater impact on the ejection's duration. In fact, the maximum Δp, which directly affects the jet penetration and then the start of combustion in the main chamber, is more sensitive to the nozzle diameter than to the volume (Fig. 6a and 8a). Finally, the variation of nozzle diameter has an important impact on the jet momentum flux (Fig. 9c), especially during the ejection. Particularly, an increase in the diameter at constant volume results in higher jet momentum, thus in a better jet penetration, in line with what is observed in Fig. 8c. Moreover, considering the smaller diameter, the jet momentum flux is particularly low, thus resulting in a very poor jet penetration, especially for the leanest case.

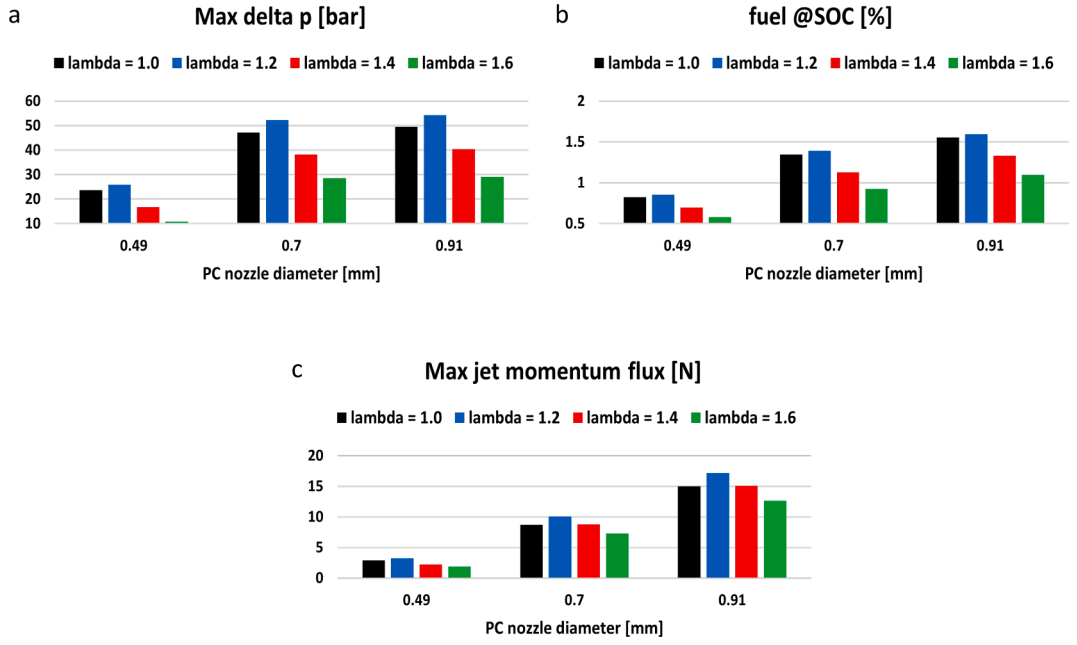

Fig. 8. Maximum Δp (a), fuel @SOC (b), and maximum jet momentum flux (c) for different values of nozzle diameter, $V_{PC} = 600$ mm^3, at 4500 rpm and different λ values.

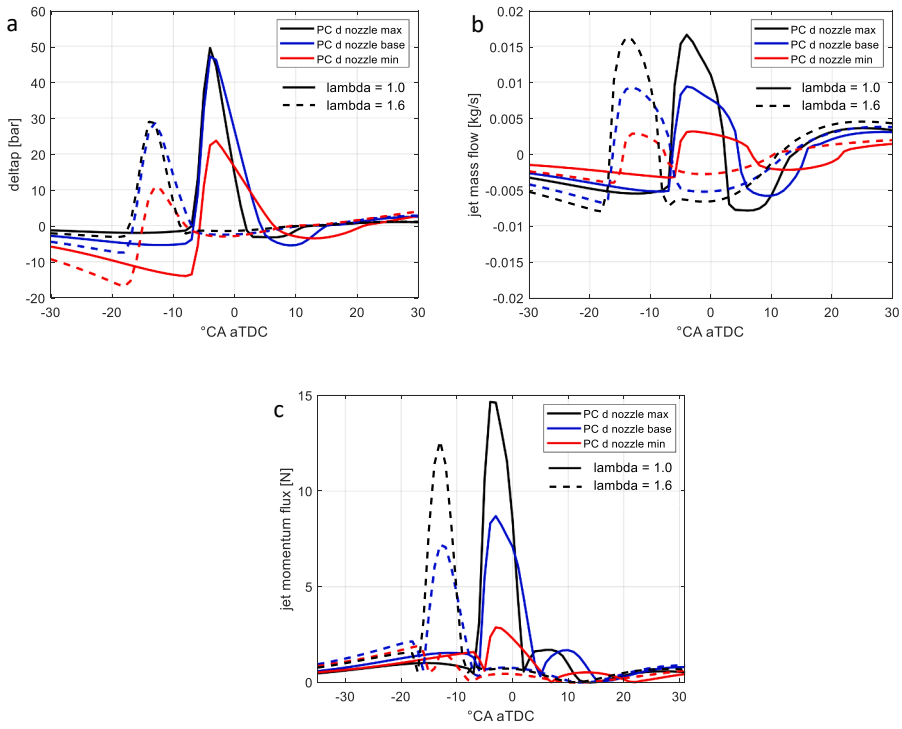

Fig. 9. Δp (a), jet mass flow rate (b), and jet momentum flux (c) for different values of nozzle diameter, $V_{PC} = 600$ mm^3, at 4500 rpm, $\lambda = 1.0$, and $\lambda = 1.6$.

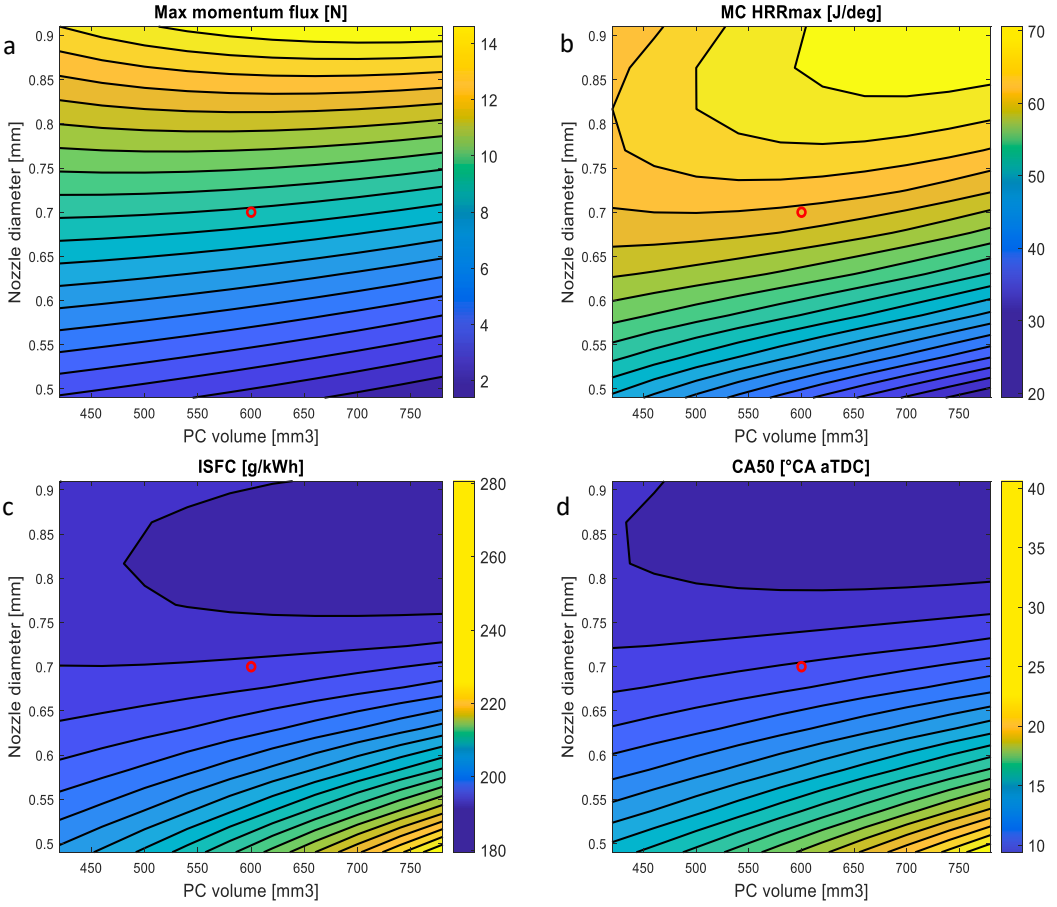

Fig. 10. Maximum jet momentum flux (a), main chamber maximum HRR (b), ISFC (c), and main chamber CA50 (d) for $\lambda = 1.0$. Red dot. base configuration ($V_{PC} = 600$ mm^3, $d_{nozzle} = 0.7$ mm). (For interpretation of the references to colour in this figure legend, the reader is referred to the web version of this article.)

4.4. Optimal prechamber design

In this section, an analysis of the impact of prechamber geometry on jet performance, main chamber combustion, and fuel consumption is presented. Particularly, the cases with $\lambda = 1.0$ and $\lambda = 1.6$ are compared with each other, to assess how the air dilution impacts the prechamber design.

It is worth noting that all the simulation for each λ value have been carried out by keeping the spark timing constant.

Fig. 10(a ÷ d) depicts the maximum jet momentum flux, the maximum HRR in the main chamber, the ISFC, and the CA50 in the main chamber as a function of the prechamber volume and the nozzle diameter, for $\lambda = 1.0$.

It is worth noting that the assessment of the main chamber maximum HRR and CA50 was possible, thanks to the predictive approach adopted to simulate the combustion process in the cylinder.

As can be observed, the best results, in terms of high values of maximum jet momentum and main chamber maximum HRR (Fig. 10a, b) and low values of ISFC and main chamber CA50 (Fig. 10c, d), are obtained for medium-to-high prechamber volumes and high nozzle diameters. In fact, large prechamber volumes together with large diameters promote the prechamber filling during the compression stroke, then maximizing the fuel @SOC. Therefore, the higher the fuel @SOC, the higher the maximum jet momentum and the better the jet penetration in the main chamber. A better jet penetration results in faster combustion (high values of maximum HRR, Fig. 10b) and a more favorable combustion phasing (low values of CA50, Fig. 10d) in the main chamber, which in turn lead to higher engine thermal efficiency, evidenced by low values of the ISFC (Fig. 10c). On the other hand, the worst performance of the prechamber is obtained for large volumes and very small diameters, as the prechamber filling is prevented and the fuel @SOC is reduced. A lower fuel @SOC results in a worse jet penetration, which results in a slower and more delayed main chamber combustion, which in turn determines an increase in fuel consumption.

It is worth noting that, in the evaluated range, all the variables represented in Fig. 10 are more sensitive to diameter than volume, as a diameter variation has a greater impact on the maximum Δp, fuel @SOC, and maximum jet momentum (Fig. 8) than a volume variation (Fig. 6). However, for nozzle diameters higher than 0.7 mm, an increased sensitivity of the aforementioned variables to the volume, especially the maximum HRR (Fig. 10 b), is observed. This can be due to the easier prechamber filling promoted by larger diameters. In fact, a better prechamber filling enhances the effect of volume variations on the fuel @SOC, then on jet penetration, main chamber combustion speed, and phasing and on fuel consumption.

In Fig. 11(a ÷ d) are presented the maximum jet momentum flux, the maximum HRR in the main chamber, the ISFC, and the CA50 in the main chamber as a function of the volume and the nozzle diameter, for $\lambda = 1.6$.

Like for $\lambda = 1.0$ (Fig. 10), also in the leanest case high values of jet maximum momentum flux (Fig. 11a) and main chamber maximum HRR (Fig. 11b), and low values of ISFC (Fig. 11c) and main chamber CA50 (Fig. 11d) are reached for medium-to-high values of prechamber volume and high nozzle diameters, confirming the similar behavior of the jet performance in the two cases observed in the previous section. However, the maximum values of maximum jet momentum and maximum HRR

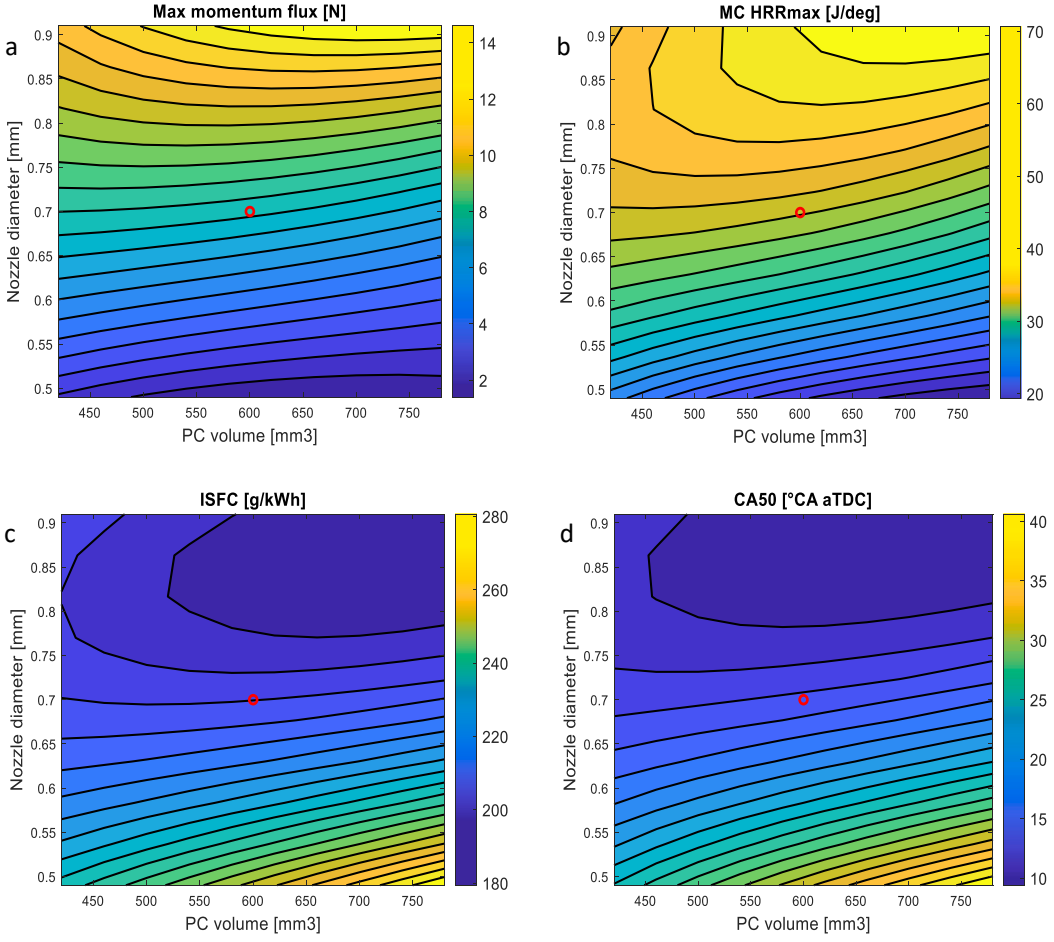

Fig. 11. Maximum jet momentum flux (a), main chamber maximum HRR (b), ISFC (c), and main chamber CA50 (d) for $\lambda = 1.6$. Red dot. base configuration ($V_{PC} = 600$ mm^3, $d_{nozzle} = 0.7$ mm). (For interpretation of the references to colour in this figure legend, the reader is referred to the web version of this article.)

(Fig. 11a, b) are lower, and the minimum values of ISFC and CA50 are higher than those observed in the case with $\lambda = 1.0$. This is ascribable to the lower energy available for the ejection at $\lambda = 1.6$, associated with the lower fuel @SOC for the leanest case. A lower energy available for the ejection results in a lower jet penetration (lower maximum jet momentum, Fig. 11a), which in turn determines a slower combustion (lower maximum HRR, Fig. 11b) and a more delayed start of combustion (higher CA50, Fig. 11d) in the main chamber. A slower and more delayed combustion justifies the slightly higher values of ISFC (Fig. 11c) for the case with $\lambda = 1.6$, with respect to the stoichiometric one, confirming what is observed in Fig. 3c. Moreover, in the leanest case, the portion of the simulated space characterized by the highest values of maximum HRR and lowest values of ISFC is smaller, if compared to the stoichiometric case (Fig. 10 b, c). In addition, the maximum HRR and the ISFC for nozzle diameters greater than 0.7 mm show a higher sensitivity to the prechamber volume, evidencing a more rapid decay of main chamber combustion velocity and engine efficiency as the volume is decreased.

5. Conclusions and future developments

An experimental and numerical analysis has been carried out to evaluate the effects of a passive TJI system on SI engine combustion and performance, in stoichiometric and lean-burn operating conditions. Particularly, a 1-D engine model was developed and validated against the experimental data, to simulate the impact of the prechamber geometry on the combustion process and engine efficiency.

Both experimental and simulation results show that, by increasing λ from 1.0 to 1.6, a combustion slowdown occurs, noticeable from the decrease in maximum HRR. Nevertheless, the TJI concept allows guaranteeing a faster combustion process than a conventional spark ignition system, particularly under a lean mixture.

Mixture leaning up to $\lambda = 1.6$ resulted in a decrease in fuel amount in the prechamber at SOC, as the advancing of the spark timing prevents the prechamber filling, which in turn induced a decrease of the maximum Δp and the maximum jet momentum. Therefore, an increase in air dilution induces a reduction of jet penetration, resulting in slower and more delayed combustion in the main chamber.

The impact of prechamber geometry has been analyzed by considering a variation of $\pm$ 30% in the prechamber A/V ratio around the base value. The results show that an increase in volume at constant diameter determines an increase in fuel at SOC with a reduction of maximum Δp, and then of maximum jet momentum. The latter, in turn, results in a reduction of the jet penetration, as smaller prechambers are filled more rapidly, thus reducing the pressure difference between the two chambers during the filling process.

On the other hand, an increase in diameter at constant volume resulted in an increase in fuel at SOC and maximum Δp, which in turn determined a higher jet momentum flux, thus improving the jet penetration. This is due to the easier prechamber filling during the compression stroke, promoted by larger diameters. Moreover, maximum Δp and maximum jet momentum are more sensitive to diameter variations rather than to volume variations, due to the greater sensitivity of the fuel at SOC to the diameter.

The effects of A/V ratio variations are similar for all the λ values investigated. However, for a given prechamber configuration, an increase in λ results in a reduction of fuel at SOC, thus in a decrease in maximum Δp and in a reduction of jet penetration. The sensitivity to λ of the fuel @SOC becomes slightly higher as the A/V ratio is increased, which leads to an increased sensitivity to the air dilution level also for the maximum Δp and the maximum jet momentum flux.

Following the jet performance analysis, the impact on the main chamber combustion process and engine efficiency has been studied. Particularly, the results evidence that medium-to-high volumes and big nozzle diameters allow achieving the best performance in terms of jet penetration (high maximum jet momentum), which in turn promotes faster and best-timed main chamber combustion (high maximum HRR and low CA50) with higher engine efficiency (low ISFC). In fact, large prechamber volumes together with large diameters promote the prechamber filling, maximizing the fuel at SOC and the energy available for the ejection.

It is worth noting that the effect of prechamber A/V ratio is not significantly affected by the air–fuel ratio. Therefore, the optimization of prechamber design can be carried out regardless of the λ value.

Future works will consider the impact of the engine speed, as well as the air dilution, on the prechamber design.

CRediT authorship contribution statement

Emmanuele Frasci: Conceptualization, Formal analysis, Investigation, Methodology, Software, Validation, Writing – original draft, Writing – review & editing. **Ricardo Novella Rosa:** Conceptualization, Formal analysis, Investigation, Methodology, Supervision, Software, Validation, Writing – original draft, Writing – review & editing. **Benjamín Plá Moreno:** Conceptualization, Formal analysis, Investigation, Methodology, Supervision, Writing – original draft, Writing – review & editing. **Ivan Arsie:** Conceptualization, Formal analysis, Investigation, Methodology, Supervision, Writing – original draft, Writing – review & editing. **Elio Jannelli:** Conceptualization, Supervision, Writing – review & editing.

Declaration of Competing Interest

The authors declare that they have no known competing financial interests or personal relationships that could have appeared to influence the work reported in this paper.

Data availability

The authors are unable or have chosen not to specify which data has been used.

References

[1] Vressner, A., Gabrielsson, P., Gekas, I., & Senar-Serra, E. (2010). Meeting the EURO VI NOx Emission Legislation using a EURO IV Base Engine and a SCR/ASC/DOC/DPF Configuration in the World Harmonized Transient Cycle (No. 2010-01-1216). SAE Technical Paper. 10.4271/2010-01-1216.

[2] Heywood JB. Internal combustion engine fundamentals. New York: McGraw- Hill Book Co.; 1988.

[3] Attard WP, Parsons P. Flame kernel development for a spark-initiated pre-chamber combustion system capable of high load, high efficiency and near zero NOx emissions. SAE Int J Engines 2010;3(2):408–27. https://doi.org/10.4271/2007-01-3623.

[4] Wang J, Chen H, Hu Z, Yao M, Li Y. A review on the Pd-based three-way catalyst. Catal Rev 2015;57(1):79–144.

[5] Irimescu A, Merola SS, Martinez S. Influence of Engine Speed and Injection Phasing on Lean Combustion for Different Dilution Rates in an Optically Accessible Wall-Guided Spark Ignition Engine. SAE Int J Engines 2018;11(6):1343–70.

[6] Attard, W. P., & Blaxill, H. (2012). *A lean burn gasoline fueled pre-chamber jet ignition combustion system achieving high efficiency and low NOx at part load* (No. 2012-01-1146). SAE Technical Paper. https://www.sae.org/publications/technical-papers/content/2012-01-1146.

[7] Yeo, G., Kil, J., Youn, Y., Kim, C., & Kim, N. (2000). *Three-way catalysts for partial lean-burn engine vehicle* (No. 2000-05-0322). SAE Technical Paper. https://www.sae.org/publications/technical-papers/content/2000-05-0322.

[8] Takami, A., Takemoto, T., Ichikawa, S., Saito, F., & Komatsu, K. (1994). Three-way catalyst for advanced lean burn engine. In: JSAE spring conference. Society of Automotive Engineers of Japan; 1994.

[9] Peterson B, Reuss DL, Sick V. On the ignition and flame development in a spray-guided direct-injection spark-ignition engine. Combust Flame 2014;161(1):240–55. https://www.sciencedirect.com/science/article/pii/S0010218013003234.

[10] Gentz G, Thelen B, Gholamisheeri M, Litke P, Brown A, Hoke J, et al. A study of the influence of orifice diameter on a turbulent jet ignition system through combustion visualization and performance characterization in a rapid compression machine. Appl Therm Eng 2015;81:399–411. https://www.sciencedirect.com/science/article/pii/S1359431115001349.

[11] Toulson, E., Schock, H. J., & Attard, W. P. (2010). A review of pre-chamber initiated jet ignition combustion systems. https://saemobilus.sae.org/content/2010-01-2263.
[12] Alvarez CEC, Couto GE, Roso VR, Thiriet AB, Valle RM. A review of prechamber ignition systems as lean combustion technology for SI engines. Appl Therm Eng 2018;128:107–20. https://www.sciencedirect.com/science/article/pii/S1359431117302284.
[13] Sementa, P., Catapano, F., Di Iorio, S. & Vaglieco, B. M. (2019). Experimental Investigation of a Fueled Prechamber Combustion in an Optical Small Displacement SI Methane Engine (No. 2019-24-0170). SAE Technical Paper. https://www.sae.org/publications/technical-papers/content/2019-24-0170.
[14] Heyne S, Meier M, Imbert B, Favrat D. Experimental investigation of prechamber autoignition in a natural gas engine for cogeneration. Fuel 2009;88(3):547–52. https://www.sciencedirect.com/science/article/pii/S0016236108003712.
[15] Attard, W. P., Bassett, M., Parsons, P., & Blaxill, H. (2011). *A new combustion system achieving high drive cycle fuel economy improvements in a modern vehicle powertrain* (No. 2011-01-0664). SAE Technical Paper. https://saemobilus.sae.org/content/2011-01-0664.
[16] Gentz G, Thelen B, Litke P, Hoke J, Toulson E. Combustion visualization, performance, and CFD modeling of a pre-chamber turbulent jet ignition system in a rapid compression machine. SAE Int J Engines 2015;8(2):538–46. https://doi.org/10.4271/2015-01-0779.
[17] Gentz G, Gholamisheeri M, Toulson E. A study of a turbulent jet ignition system fueled with iso-octane: pressure trace analysis and combustion visualization. Appl Energy 2017;189:385–94.
[18] Chinnathambi, P., Bunce, M., & Cruff, L. (2015). *RANS based multidimensional modeling of an ultra-lean burn pre-chamber combustion system with auxiliary liquid gasoline injection* (No. 2015-01-0386). SAE Technical Paper. https://saemobilus.sae.org/content/2015-01-0386.
[19] Biswas S, Tanvir S, Wang H, Qiao L. On ignition mechanisms of premixed CH4/air and H2/air using a hot turbulent jet generated by pre-chamber combustion. Appl Therm Eng 2016;106:925–37. https://www.sciencedirect.com/science/article/pii/S135943111630984X.
[20] Allison PM, De Oliveira M, Giusti A, Mastorakos E. Pre-chamber ignition mechanism: experiments and simulations on turbulent jet flame structure. Fuel 2018;230:274–81. https://www.sciencedirect.com/science/article/pii/S0016236118308287.
[21] Attard WP, Blaxill H. A single fuel pre-chamber jet ignition powertrain achieving high load, high efficiency and near zero NOx emissions. SAE Int J Engines 2012;5(3):734–46. https://saemobilus.sae.org/content/2011-01-2023.
[22] Attard WP, Blaxill H, Anderson EK, Litke P. Knock limit extension with a gasoline fueled pre-chamber jet igniter in a modern vehicle powertrain. SAE Int J Engines 2012;5(3):1201–15. https://saemobilus.sae.org/content/2012-01-1143.
[23] Attard, W. P., Toulson, E., Huisjen, A., Chen, X., Zhu, G., & Schock, H. (2012). *Spark ignition and pre-chamber turbulent jet ignition combustion visualization* (No. 2012-01-0823). SAE Technical Paper. 10.4271/2012-01-0823.
[24] Vedula RT, Gentz G, Stuecken T, Toulson E, Schock H. Lean burn combustion of Iso-Octane in a rapid compression machine using dual mode turbulent jet ignition system. SAE Int J Engines 2018;11(1):95–108. https://doi.org/10.4271/03-11-01-0007.
[25] Sens M, Binder E. Pre-chamber ignition as a key technology for future powertrain fleets. MTZ worldwide 2019;80(2):44–51. https://doi.org/10.1007/s38313-018-0150-1.
[26] Xu G, Kotzagianni M, Kyrtatos P, Wright YM, Boulouchos K. Experimental and numerical investigations of the unscavenged prechamber combustion in a rapid compression and expansion machine under engine-like conditions. Combust Flame 2019;204:68–84. https://www.sciencedirect.com/science/article/abs/pii/S0010218019300434.
[27] Wang, N., Liu, J., Chang, W. L., & Lee, C. F. (2018). A numerical study of the combustion and jet characteristics of a hydrogen fueled turbulent hot-jet ignition (THJI) chamber. international journal of hydrogen energy, 43(45), 21102-21113. Doi: 10.1016/j.ijhydene.2018.09.156.
[28] Attard WP, Parsons P. A normally aspirated spark-initiated combustion system capable of high load, high efficiency and near zero NOx emissions in a modern vehicle powertrain. SAE Int J Engines 2010;3(2):269–87. https://doi.org/10.4271/2010-01-2196.
[29] Frasci, E., Sementa, P., Arsie, I., Jannelli, E., & Vaglieco, B. M. (2021). *Experimental and Numerical Investigation of a Lean SI Engine To Be Operated as Range Extender for Hybrid Powertrains* (No. 2021-24-0005). SAE Technical Paper. 10.4271/2021-24-0005.
[30] López JJ, Novella R, Gómez-Soriano J, Martinez-Hernandiz PJ, Rampanarivo F, Libert C, et al. Advantages of the unscavenged pre-chamber ignition system in turbocharged natural gas engines for automotive applications. Energy 2021;218:119466. https://doi.org/10.1016/j.energy.2020.119466.
[31] Benajes, J., Novella, R., Gomez-Soriano, J., Martinez-Hernandiz, P., Libert, C., & Dabiri, M. (2019). Performance of the passive pre-chamber ignition concept in a spark-ignition engine for passenger car applications. Proceedings of the SIA Powertrain Electronics, Paris, France, 12–13.
[32] Novella, R., Pastor, J., Gomez-Soriano, J., Barbery, I., Libert, C., Rampanarivo, F., ... & Dabiri, M. (2020). Experimental and numerical analysis of passive pre-chamber ignition with EGR and air dilution for future generation passenger car engines (No. 2020-01-0238). SAE Technical Paper. 10.4271/2020-01-0238.
[33] Benajes J, Novella R, Gómez-Soriano J, Martinez-Hernandiz PJ, Libert C, Dabiri M. Evaluation of the passive pre-chamber ignition concept for future high compression ratio turbocharged spark-ignition engines. Appl Energy 2019;248:576–88. https://doi.org/10.1016/j.apenergy.2019.04.131.
[34] GT-Suite Engine performance application manual, Gamma Technologies.
[35] Wenig, M., Roggendorf, K., & Fogla, N. (2019, June). Towards predictive dual-fuel combustion and prechamber modeling for large two-stroke engines in the scope of 0D/1D simulation. In *Proceedings of the 29th CIMAC world congress on combustion engine technology, Vancouver, BC, Canada* (pp. 10-14).
[36] Ouellette PHPG, Hill PG. Turbulent transient gas injections. J Fluids Eng 2000;122(4):743–52. https://doi.org/10.1115/1.1319845.
[37] Wahiduzzaman S, Morel T, Sheard S. Comparison of measured and predicted combustion characteristics of a four-valve SI engine. SAE Trans 1993:810–9. https://www.jstor.org/stable/44611419.
[38] Irimescu, A., Catapano, F., Di Iorio, S., Merola, S., Sementa, P., & Vaglieco, B. M. (2018). Quasi-Dimensional Simulation of Downsizing and Inverter Application for Efficient Part Load Operation of Spark Ignition Engine Driven Micro-Cogeneration Systems (No. 2018-32-0061). SAE Technical Paper. 10.4271/2018-32-0061.
[39] Fogla N, Bybee M, Mirzaeian M, Millo F, Wahiduzzaman S. Development of a K-k-ϵ phenomenological model to predict in-cylinder turbulence. SAE Int J Engines 2017;10(2):562–75. https://doi.org/10.4271/2017-01-0542.
[40] Woschni, G. (1967). A universally applicable equation for the instantaneous heat transfer coefficient in the internal combustion engine (No. 670931). SAE Technical paper. 10.4271/670931.
[41] Shah, A., Tunestal, P., & Johansson, B. (2015). Effect of pre-chamber volume and nozzle diameter on pre-chamber ignition in heavy duty natural gas engines (No. 2015-01-0867). SAE Technical paper. 10.4271/2015-01-0867.